ADVANCED PHOTONICS RESEARCH
Open Access
www.adpr-journal.com

Multiple Incoherent Deconvolutions for Improving the Image Resolution of Diffraction-Limited Imaging Systems

Jawahar Prabhakar Desai, Vijayakumar Anand, and Joseph Rosen*

A new method of imaging with enhanced resolution beyond the diffraction limit is proposed and demonstrated. The target is imaged multiple times, each time with a different phase mask on the aperture of the imaging system. Nonlinear Wiener deconvolution (NWD) reconstructs each image according to the corresponding aperture, and as a result, an image of the target with improved resolution is obtained. The relatively high noise level of each resulting image is eliminated by averaging the multiple deconvolution results. NWD is compared to linear Wiener deconvolution with and without different phase masks. System users can tune the number of imaging events as a tradeoff between low noise and high resolution and between low noise and a low number of camera shots.

1. Introduction

The challenge of seeing as many tiny details as possible in an image has attracted the interest of many researchers worldwide for many years. The principles behind the various methods of resolution improvement (frequently called superresolution methods) derive from the well-known diffraction limit, which states that the minimal resolved size δ is the ratio between half the wavelength of the illumination light, λ, and the system's numerical aperture, NA, formulated as $\delta = \lambda/(2NA)$.[1] One strategy for viewing small details beyond these limitations is to reduce the illumination wavelength and adjust the optical components and detectors of the imaging instrument to the reduced wavelength.[2] However, the wavelength is not always controllable since the observed target might emit self-illumination light at a given unchangeable wavelength. Furthermore, manufacturing optics for wavelengths shorter than visible wavelengths requires engineering and processing of materials for which advanced manufacturing technologies have not reached industry standards, such as those in the visible region. The second category of superresolution methods, also implied from the abovementioned relation, includes all the techniques for increasing the physical or effective numerical apertures. This category has been well studied in the past 150 years since the pioneering works of Rayleigh[3] and Abbe.[4]

Familiar examples of this category include systems with synthetic apertures,[5–8] structured illumination techniques,[9–12] holographic methods,[13,14] and scattering masks between a target and the input of the observing device.[15,16] However, these methods of increasing the physical or effective numerical aperture are not always possible, and interesting questions addressed herein are whether and how the image resolution can be improved in a system with a given, unchangeable, numerical aperture, and wavelength.

Many studies have supported the claim that the resolution can be improved even though the numerical aperture and wavelength cannot be changed. Therefore, the third category of improving the resolution involves techniques in which both the wavelength and the numerical aperture are a priori given and cannot be modified. Methods of spatial filtering,[17–19] incoherent self-interference holography,[20–22] image deconvolution,[23–25] and postprocessing by the Gerchberg algorithm[26] or similar algorithms[27,28] meet this challenge of improving the resolution in a system with an unchangeable numerical aperture and wavelength. With all these techniques, the resolution can be significantly improved such that the minimal resolved size is below the abovementioned diffraction limit. Most of the methods in the third category follow the property that the object occupies a small area out of the overall field of view. This property guarantees that leftovers of high-frequency information beyond the cutoff frequency of the imaging system (tails of bell-like spectral functions) are still detected and can be used to estimate the object's spectra beyond the cutoff frequency. Generally, techniques in the third category suffer from relatively low signal-to-noise ratios (SNRs).[29] More promising resolution enhancement methods, considered herein as the fourth category, extend the system dimensions from space alone to space and additional dimensions. Examples of the use of an extension of dimensions from space to space time include photoactivated localization

J. P. Desai, J. Rosen
School of Electrical and Computer Engineering
Ben Gurion University of the Negev
Beer-Sheva 8410501, Israel
E-mail: jawaharp@post.bgu.ac.il

V. Anand
Institute of Physics
University of Tartu
W. Ostwaldi 1, 50411 Tartu, Estonia

V. Anand
Optical Sciences Center
Swinburne University of Technology
Hawthorn, Melbourne, VIC 3122, Australia

The ORCID identification number(s) for the author(s) of this article can be found under https://doi.org/10.1002/adpr.202400141.

DOI: 10.1002/adpr.202400141

microscopy[30,31] and stochastic optical reconstruction microscopy.[32,33] In both techniques, the random emission of fluorescent pulses from each tiny light source over time is recorded and digitally processed to localize the sources.

The methods proposed in this study belong to the fourth category in terms of dimension addition, fixed illumination wavelengths, and unalterable numerical apertures. In this method, images are processed beyond the input lens (objective lens in microscopes) such that the system's numerical aperture is already determined by the input lens and remains unchangeable. The dimensions of the processing procedure are extended from space only to space and the state of the system's aperture. This means that various phase masks are positioned in the system aperture such that a different image is recorded for a different phase mask in every camera shot. The collection of images contains two-dimensional (2D) spatial information accumulated along the additional dimension of the system's aperture state, overall creating a three-dimensional space of information. Each image for each system's aperture is recovered by a deconvolution process, and all the deconvolution results are averaged to a single output image. To further increase the resolution, we propose processing the images with a new type of nonlinear deconvolution, which is defined below. Since multiple images are captured by incoherent optical systems and processed by nonlinear deconvolutions, we call this technique multiple incoherent nonlinear deconvolutions (MIND) and compare it to the method of multiple incoherent linear deconvolutions (MILD). By this technique, the deconvolution of each image provides resolution enhancement, and averaging over the deconvolution results, along the additional dimension of the aperture state, increases the SNR in comparison to a single deconvolution. In other words, the inherent weakness of the relatively low SNR, which is typical for methods from the third category,[29] is eliminated in both MIND and MILD by multiple measurements for different system aperture states.

The combination of nonlinear deconvolution and averaging was recently proposed for endoscopy applications,[34] but MIND is different from that study in several aspects. The main difference is that the system has the same open aperture for all multiple images.[34] Thus, only the detection noise generated by the digital camera is reduced, not any other significant noise. Superresolution methods using multiple coded aperture masks have been proposed in recent studies,[35,36] but these methods overcome the geometrical resolution limitation dictated by the pixel size of the camera. Few studies have used multiple coded aperture masks to increase the resolution of a diffraction-limited imaging system.[37–39] However, only linear Wiener filtering was applied in these studies,[36,38] and no mechanism for eliminating noise was proposed. In contrast, in the present study, we use nonlinear Wiener deconvolution (NWD) and compare its performance to that of linear Wiener deconvolution (LWD); additionally, we suggest a way to reduce the noise from the image with the ability to choose the tradeoff between high resolution and low noise. MIND can be applied for other deconvolution-based applications, such as imaging through a scattering medium, if multiple point spread functions (PSFs) are known for the deconvolution algorithm. A similar algorithm to MIND has already been applied to noninvasive imaging through a scattering medium[40]; this method is similar to MIND in the sense that both capture multiple images passing through different apertures, but the images are reconstructed by a different algorithm and are averaged to a final image.

As mentioned above, in MIND, a set of different phase masks is used as the system aperture in an incoherent optical system. The use of optical masks to improve resolution is a well-known practice in optical microscopy. Optical masks are utilized in three main superresolution methods. The first is structured illumination,[9–12] where the masks are located between the light source and the sample. The second is light scattering in front of the objective,[15,16] where the masks are located between the sample and the microscope objective. The third is spatial filtering,[17–19] which includes MIND and MILD, where the masks are positioned beyond the objective lens. In the first two mask locations, the effective *NA* is extended, but in the third mask location, the *NA* cannot be changed effectively or physically. MIND and MILD belong to the family of spatial filtering techniques,[17–19] but their new aspect is dynamic filtering with multiple filters. Therefore, the SNR of multiple deconvolution images, as we show below, is improved compared to that of a single-shot spatial filtering technique.

Another significant aspect of MIND is nonlinear deconvolution, which is performed for every captured image; hence, it seems appropriate to comment on the nonlinearity of the deconvolution in general.[41–45] Nonlinear deconvolutions are valid if their behavior is similar to that of a pseudolinear shift-invariant process. This means that although the mathematical operation is nonlinear, such that the superposition property is not valid, any target point located anywhere in the input plane is recovered independently of the other target points. In other words, the superposition property mathematically and theoretically does not exist but practically does exist in many experiments with everyday imaged targets. These pseudolinear shift-invariant characteristics of the nonlinear deconvolutions are achieved if and when the nonlinearity operates on the target's spectral magnitude only, where the spectral phase is processed linearly by multiplication with a phase filter. For many real-world targets, most of the object information is in the spectral phase distribution.[46] Therefore, because the nonlinear operation is performed on the spectral magnitude and the spectral phase is treated linearly, the nonlinear deconvolutions show pseudolinear and shift-invariant behavior. In fact, the success of nonlinear deconvolutions in recovering images of general targets is additional evidence for the claim that most of the target's visual information is stored in the spectral phase distribution. However, in some special cases, the target information is in the spectral magnitude rather than in the phase, and in these cases, some of the nonlinear deconvolutions might not work. As an example of such a special case, let us look at a periodic grid of points or an arbitrary object duplicated on a periodic grid of points (the object function is convolved with the grid of points). For an infinite grid of infinitesimal points that can be formally described as a grid of delta functions, the Fourier transform of the grid is a different grid of delta functions with a different cycle, which is a positive real-valued spectral function with a constant phase value. Any nonlinear operation that replaces the magnitude with a different distribution from the original spectral grid might not maintain the image information of the original grid of points. There are other special examples in which the spectral magnitude contains

all the target information, but these examples rarely appear in real life. Nevertheless, one should be aware of these special cases and implement nonlinear methods with special care. Fortunately, the nonlinear deconvolutions proposed in the past[41–45] and the current proposed algorithm are based on an optimization in which linear deconvolutions exist in the solution space of the algorithms as legitimate solutions. Therefore, even for the abovementioned special cases, we can expect that nonlinear deconvolution algorithms will converge during the optimization process to linear deconvolution solutions.

In the next section, we introduce MIND and its theory. Simulations and experiments of MIND in comparison to MILD and to a method with the same open aperture without phase masks are presented in the third and fourth sections, respectively. The article is summarized in the fifth section.

2. Methodology

MIND is a method of imaging with enhanced resolution based on K imaging events, each time with a different phase mask displayed on the system's aperture. The suggested configuration is shown in **Figure 1**, where beyond the input lens L_A, at a distance d from it, there is a phase mask attached to a spherical positive lens. Several constraints dictate the design of the system. First, the object should be imaged directly on the camera plane, with controllable magnification, by two lenses, one refractive L_A and the other diffractive L_B. The phase mask is displayed on the same spatial light modulator (SLM) with the diffractive lens L_B and should be illuminated by a collimated beam. In addition, when a point source illuminates the system, the intensity on the camera plane should be relative to the square magnitude of the Fourier transform of the phase mask. Under all these constraints, the object plane is at the forward focus of the L_A ($z_o = f_A$, the focal length of the lens L_A), and the camera is at the back focus of the L_B ($z_i = f_B$, the focal length of the lens), where the image magnification is z_i/z_o. The distance d can be zero, but because the SLM is reflective, d should be long enough to contain the beamsplitter and the polarizer shown in Figure 9. In the following experiment, the mask and the lens are combined into a single diffractive element displayed on the SLM. The SLM enables the display of K computer-generated phase masks on the system aperture, and as a result, K different images are recorded by the digital camera. Each of the K images is processed by nonlinear deconvolution, and the K deconvolution results are averaged over the final image. In general, any type of deconvolution is supposed to improve image resolution. This is because the modulation transfer function (MTF) of an incoherent imaging system with an open disk-like aperture has a cone-like shape in which the low frequencies are amplified more than the high frequencies. The effect of the deconvolution compensates for the unequal amplification of the MTF by amplifying the distribution at high frequencies more than at low frequencies. Consequently, tiny details blurred in the raw images are emphasized as the result of the deconvolution. As we have shown below, nonlinear deconvolution enhances the effect of resolution improvement since the algorithm searches for optimal parameters that minimize a cost function whose minimum is supposed to represent relatively high image resolution.

In Wiener deconvolution,[1,47] the system's response $f(\bar{\boldsymbol{r}})$ for the input object is deconvolved with the PSF of the imaging system $p(\bar{\boldsymbol{r}})$. Formally, the result of deconvolution is given as follows:

$$R(\bar{\boldsymbol{r}};w) = f(\bar{\boldsymbol{r}}) * h(\bar{\boldsymbol{r}}) = \mathcal{F}^{-1}\left\{|F(\bar{\boldsymbol{v}})|\exp(i\Phi_F(\bar{\boldsymbol{v}}))\cdot\frac{|P(\bar{\boldsymbol{v}})|\exp(-i\Phi_P(\bar{\boldsymbol{v}}))}{|P(\bar{\boldsymbol{v}})|^2 + c}\right\} \quad (1)$$

where c is a constant, $*$ is a 2D convolution, $\bar{\boldsymbol{r}}$ is the location vector in the object plane, $\bar{\boldsymbol{v}}$ is the spatial frequency vector, $F(\bar{\boldsymbol{v}}) = |F(\bar{\boldsymbol{v}})|\exp(i\Phi_F(\bar{\boldsymbol{v}})) = \mathcal{F}\{f(\bar{\boldsymbol{r}})\}$, $P(\bar{\boldsymbol{v}}) = |P(\bar{\boldsymbol{v}})|\exp(i\Phi_P(\bar{\boldsymbol{v}})) = \mathcal{F}\{p(\bar{\boldsymbol{r}})\}$, and $h(\bar{\boldsymbol{r}}) = \mathcal{F}^{-1}\{|P|\exp(-i\Phi_P)/[|P(\bar{\boldsymbol{v}})|^2 + c]\}$, where $F$and F^{-1} are Fourier and inverse Fourier transforms, respectively. The deconvolved result approaches the original object as c approaches $N(\bar{\boldsymbol{v}})/S(\bar{\boldsymbol{v}})$, where $S(\bar{\boldsymbol{v}})$ and $N(\bar{\boldsymbol{v}})$ are the power spectral densities of the original object and the noise, respectively.

Nonlinear reconstruction (NLR)[41] is another technique for recovering the image of the original object, where the amplitudes

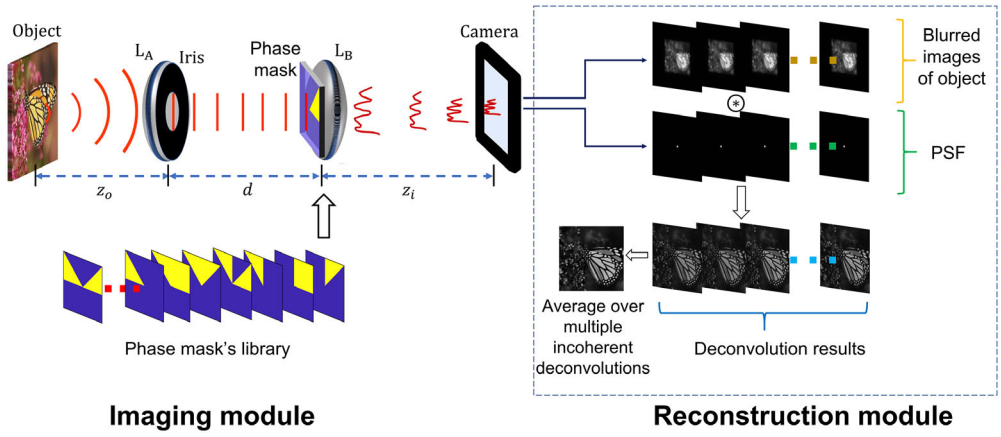

Figure 1. Conceptual layout of the MIND. Multiple incoherent nonlinear deconvolution (on the left) optical incoherent imaging system with binary phase masks at the aperture and a reconstruction module (on the right, shown in the dotted box). ⊛ indicates nonlinear deconvolution, and PSF is the point spread function.

of $F(\overline{\boldsymbol{\upsilon}})$ and $P(\overline{\boldsymbol{\upsilon}})$ are raised to powers o and r, respectively. The parameters o and r are varied in the interval $[-1, 1]$. The NLR recovered image is given by the following equation:

$$N(\overline{\mathbf{r}}; o, r) = f(\overline{\mathbf{r}}) \odot p(\overline{\mathbf{r}}) = F^{-1}\{|F|^{o}\exp(i\Phi_{\mathrm{F}}) \cdot |P|^{r}\exp(-i\Phi_{\mathrm{P}})\} \tag{2}$$

where $\odot$ is a nonlinear correlation. The noisy experimental environment and selection of the cost function yield a recovered image that is less optimal than those obtained by the other deconvolution algorithms proposed herein. The aim is to reconstruct each object point as sharply as possible and to enhance the SNR. The first requirement is fulfilled for $o + r = 0$, whereas the second one is satisfied in the case of the matched filter where $o = r = 1$. Therefore, o and r are searched in the range of $[-1,1]$ to obtain the optimal reconstruction of the object.

The nonlinear deconvolution chosen in the current study is a new type of nonlinear deconvolution called NWD, which is a combination of Wiener deconvolution and NLR; thus, the combined algorithm is intended to yield a solution better than the solution of each algorithm alone, but in the worst case, the LWD can be a legitimate solution of the optimization algorithm if the cost function's minimum is obtained for LWD. The NWD, like the NLR, is a pseudolinear deconvolution because only the target's spectral magnitude of the input object is nonlinearly processed. Formally, we define the property of pseudolinearity in the deconvolution as follows. If for a single point in the system input located at $\overline{\mathbf{r}}_{\mathbf{s}}$ and represented by the delta function $\delta(\overline{\mathbf{r}} - \overline{\mathbf{r}}_{\mathbf{s}})$, the system output is $[\delta(\overline{\mathbf{r}} - \overline{\mathbf{r}}_{\mathbf{s}}) * p(\overline{\mathbf{r}})] \circledast p(\overline{\mathbf{r}}) = C \cdot \tilde{\delta}(\overline{\mathbf{r}} - M\overline{\mathbf{r}}_{\mathbf{s}})$, then the deconvolution is pseudolinear if, for multipoint input, the system output is

$$\left[\sum_{\mathrm{s}} A_{\mathrm{s}}\delta(\overline{\mathbf{r}} - \overline{\mathbf{r}}_{\mathbf{s}}) * p(\overline{\mathbf{r}})\right] \circledast p(\overline{\mathbf{r}}) \cong \sum_{\mathrm{s}}[A_{\mathrm{s}}\delta(\overline{\mathbf{r}} - \overline{\mathbf{r}}_{\mathbf{s}}) * p(\overline{\mathbf{r}}) \circledast p(\overline{\mathbf{r}})] = \sum_{\mathrm{s}} C_{\mathrm{s}} \cdot \tilde{\delta}(\overline{\mathbf{r}} - M\overline{\mathbf{r}}_{\mathbf{s}}) \tag{3}$$

where $*$ and $\circledast$ are the 2D convolution and NWD (defined in Equation (4)), respectively; $p(\overline{\mathbf{r}})$ is the PSF of the imaging system; s is the index of the object points, A_{s} ,C_{s} , and C are constants; M is the transverse magnification; and $\tilde{\delta}$ is a delta-like function such that $\tilde{\delta} = 1$ at $\overline{\mathbf{r}} = (0, 0)$ and $\tilde{\delta} \cong 0$ at elsewhere.

Next, we present the definition of NWD. The two input functions of the NWD operator are the PSF of the imaging system $p(\overline{\mathbf{r}})$ and the system's response $f(\overline{\mathbf{r}})$, which is the response to the input target $t(\overline{\mathbf{r}})$ such that $f(\overline{\mathbf{r}}) = t(\overline{\mathbf{r}}) * p(\overline{\mathbf{r}})$. The output result of NWD is as follows:

$$D(\overline{\mathbf{r}}; o, r, w) = f(\overline{\mathbf{r}}) \circledast p(\overline{\mathbf{r}}) = \mathcal{F}^{-1}\left\{|F|^{o}\exp(i\Phi_{\mathrm{F}}) \cdot \frac{|P|^{r}}{|P|^{2} + w}\exp(-i\Phi_{\mathrm{P}})\right\} \tag{4}$$

where $|P|\exp(i\Phi_P)$ and $|F|\exp(i\Phi_F)$ are Fourier transforms of $p(\overline{\mathbf{r}})$ and $f(\overline{\mathbf{r}})$, respectively. The parameters o, r, and w are searched to minimize the cost function. The o and r values are in the ranges $[-1,1]$ and $[1,3]$, respectively. The range of o includes all the linear filters ($o = 1$), and in the group of linear filters, one can find the matched filter at one end of r, $(o, r, w) = (1, 3, 0)$; the inverse filter at the other end of r, $(o, r, w) = (1, 1, 0)$; and the linear Wiener deconvolution for $(o, r) = (1, 1)$ and $w \neq 0$. The parameter w is searched around the value $N(\overline{\boldsymbol{\upsilon}})/S(\overline{\boldsymbol{\upsilon}})$. When w is added as the third variable in NWD, the deconvolution becomes a function of three parameters, which are o, r, and w. This extended dimension can lead to a better reconstruction with sharp object points and minimum noise. The necessity of NWD can be realized because NWD and LWD have one common solution, but the solution space of NWD is much wider and leads to an optimal solution that does not exist in LWD. Equating Equation (1) with (4), the result is $(|P|^2 + c)|F|^{o-1}|P|^{r-1} = |P|^2 + w$. To obtain a solution in which $w = c$, either $o = r = 1$ or both $|F|$ and $|P|$ are binary matrices with values of 0 or 1, conditions that cannot be fulfilled for realistic Fourier magnitudes. Therefore, the LWD and NLR are possible solutions in the much wider space of NWD solutions; hence, the NWD deconvolution result can yield optimal solutions that might not exist in the NLR or WD.

The optimal parameters o, r, and w of Equation (4) are determined as the values at which the cost function is minimal. The chosen cost function in the present study is the referenceless entropy function,[41] which provides a measure of disorder to the image. The assumption behind using entropy as a cost function is that without knowing the ideal input image, at the minimum entropy, the output image is "ordered" maximally; hence, this image is as close as possible to the ideal image of the object. The analog model herein is a box of gas particles creating an "image" of, for example, some grid. When the particles are uniformly distributed in the box, the entropy is maximal, and the visibility of the image is minimal, close to zero. Hence, the image similarity to the desired grid is also minimal. However, when the particles are ordered in the shape of a grid, the entropy becomes minimal. The entropy cannot approach the global minimum (which is a delta function) because, according to Equation (4), the output of the NWD, $D(\overline{\mathbf{r}}; o, r, w)$, is an image close to the target, in our example, the grid. Other cost functions for nonlinear deconvolutions have been proposed,[16,42] but for the current purpose of investigating the efficiency of NWD compared to LWD, the entropy function seems to be a good choice, although research on other cost functions remains possible in the future. The entropy function is as follows:[41]

$$E(o, r, w) = -\iint [g(\overline{\mathbf{r}}; o, r, w)] \log [g(\overline{\mathbf{r}}; o, r, w)] d\overline{\mathbf{r}} \tag{5}$$

where

$$g(\overline{\mathbf{r}}; o, r, w) = |D(\overline{\mathbf{r}}; o, r, w)| \Big/ \iint |D(\overline{\mathbf{r}}; o, r, w)| d\overline{\mathbf{r}}$$

A linear search technique is adopted to find the optimal values of o, r, and w. The o and r values are in the ranges $[-1,1]$ and $[1,3]$, respectively, whereas w is in the interval $[a_0, a_N]$ subtended around $N(\overline{\boldsymbol{\upsilon}})/S(\overline{\boldsymbol{\upsilon}})$. The flowchart for this search technique is shown later. $Entropy_{min}$ is the entropy of the optimum deconvolved image with LWD (**Figure 2**).

In the following simulation studies, we compare the NWD-based method MIND with the LWD-based MILD using two figures of merit, the entropy and structural similarity index

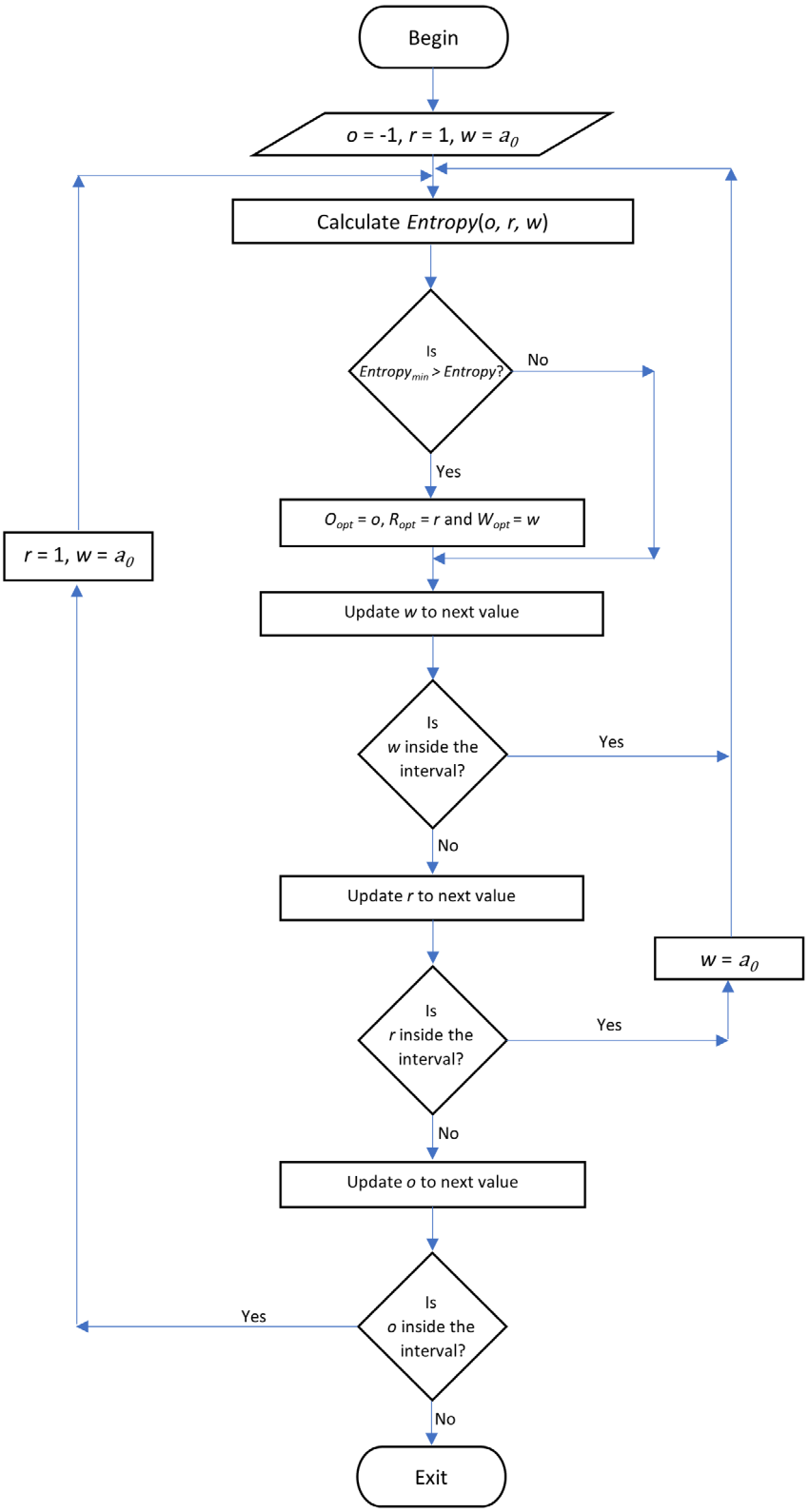

Figure 2. Flowchart for MIND. The optimal values are $o = O_{opt}$, $r = R_{opt}$, *and* $w = W_{opt}$.

(SSIM).[48] In the experimental comparison, because a part of the resolution chart is used as an observed object, we use the visibility of the smallest grating as a more direct measure of the resolution.

Next, we analytically explain the MIND algorithm. A deconvolution of a single image in the output of a diffraction-limited incoherent system can improve the image resolution, but two types of noise are added to the output image, which makes the image unsuitable for any practical purpose. The first type of noise is detection noise, which usually appears to varying degrees in images recorded by commercial digital cameras. Because the distribution of the high frequencies is amplified by the deconvolution filter and because the signal in this spectral region might be weaker than the noise, the noise might be amplified above the image signal in some regions of the picture. The detection noise can be eliminated by averaging multiple images recorded over time with the same system aperture. However, the second type of noise resulting from the deconvolution process is dependent on the system's aperture and hence cannot be eliminated by averaging multiple images with the same system aperture. The second type of noise is caused by the PSF of the deconvolution process. In general, this PSF might have tails with relatively high energy around the central lobe, which might cause images to contain unacceptable noise. To eliminate this noise by averaging, one needs to average multiple different deconvolution results, each of which is recorded with a different PSF and hence with a different system aperture. The mathematical description of MIND starts with the kth intensity response $I_k(\bar{\boldsymbol{r}})$ of a general incoherent linear system, which is the convolution between the object function $t(\bar{\boldsymbol{r}})$ and the kth PSF $p_k(\bar{\boldsymbol{r}})$ plus the detection noise $N_D(\bar{\boldsymbol{r}})$, as follows:[49]

$$I_k(\bar{\boldsymbol{r}}) = t(\bar{\boldsymbol{r}}) * p_k(\bar{\boldsymbol{r}}) + N_D(\bar{\boldsymbol{r}}) \tag{6}$$

According to the analysis of incoherent imaging systems, the k-th PSF $p_k(\bar{\boldsymbol{r}})$ is related to the k-th aperture phase mask $M_k(\bar{\boldsymbol{\rho}})$ by the following equation:[50]

$$p_k(\bar{\boldsymbol{r}}) = |\mathcal{F}^{-1}\{M_k(\lambda z_i \bar{\boldsymbol{v}})\}|^2 \tag{7}$$

where $\bar{\boldsymbol{\rho}}$ is the location vector in the aperture plane and z_i is the distance between the output aperture of the optical system and the digital camera. In principle, $p_k(\bar{\boldsymbol{r}})$ can represent any PSF function, and the aperture phase mask $M_k(\bar{\boldsymbol{\rho}})$ can represent any passive aperture with a magnitude in the range of [0,1] and a phase function with any rank of scattering limited only by the pixel size of the SLM. However, since the overall goal here is imaging, $p_k(\bar{\boldsymbol{r}})$ should be as narrow as possible but different from any other $p_l(\bar{\boldsymbol{r}})$ for any $l \neq k$.

To meet these constraints and generate K different PSFs, a systematic technique is adopted in this study, and we divide the system aperture into q (here, $q = 8$) segments, as shown in **Figure 3**a. These sections are named b_0–b_7. If we consider each sector (b_s) to represent a bit of a binary number, then b_0–b_7 can represent an eight-bit binary number, with b_7 as the most significant bit (MSB) and b_0 as the least significant bit (LSB). This aperture is to be used as a phase mask; therefore, we use 0 and π instead of 0 and 1, such that each sector (b_s) can have a value of either 0 or π. In this way, a total of 256 distinct binary phase patterns can be created; hence, there are 256 states of the system aperture. Notably, two complementary phase patterns have equal PSFs; therefore, from the 256 states of the system aperture, only 128 different PSFs can be generated. Owing to the cyclic structure of the phase pattern, the number of distinct PSFs further decreases to 85. The advantage of one phase pattern over the other is not tested here; we used them serially without prioritizing. However, the superiority of any phase mask over the other is still unclear and requires further investigation. (see several examples of phase masks in Figure 3b). Notably, this way of creating K different phase masks is arbitrary but well-reasoned, and other methods and masks might operate as well as the chosen series of masks.

After K images $I_k(\bar{\boldsymbol{r}})$ obtained via Equation (6) are recorded, the MIND algorithm is digitally calculated. In MIND, the kth deconvolution image $I_{D,k}(\bar{\boldsymbol{r}})$ is

$$\begin{aligned} I_{D,k}(\bar{\boldsymbol{r}}) &= I_k(\bar{\boldsymbol{r}}) \circledast p_k(\bar{\boldsymbol{r}}) \cong I_k(\bar{\boldsymbol{r}}) \otimes \tilde{p}_k(\bar{\boldsymbol{r}}) \\ &= [t(\bar{\boldsymbol{r}}) * p_k(\bar{\boldsymbol{r}})] \otimes \tilde{p}_k(\bar{\boldsymbol{r}}) + N_D(\bar{\boldsymbol{r}}) \otimes \tilde{p}_k(\bar{\boldsymbol{r}}) \\ &= t(\bar{\boldsymbol{r}}) * \tilde{\delta}(\bar{\boldsymbol{r}}) + N_{P,k}(\bar{\boldsymbol{r}}) + N_{D,k}(\bar{\boldsymbol{r}}) \end{aligned} \tag{8}$$

where $\otimes$ is the linear correlation, $\tilde{p}_k(\bar{\boldsymbol{r}})$ is the PSF of the deconvolution, $N_{P,k}(\bar{\boldsymbol{r}})$ is the noise caused by the k-th PSF of the system and the kth PSF of the deconvolution, and $N_{D,k}(\bar{\boldsymbol{r}})$ is the noise created from the cross-correlation between the detection noise and the k-th PSF of the deconvolution. Because the nonlinear correlation operates only on the magnitude of the input spectrum, the nonlinear correlation has a characteristic pseudolinear correlation, as discussed in the introduction and the paragraph containing Equation (3). Therefore, the approximation sign $\cong$ in Equation (8) is valid, and the nonlinear correlation is

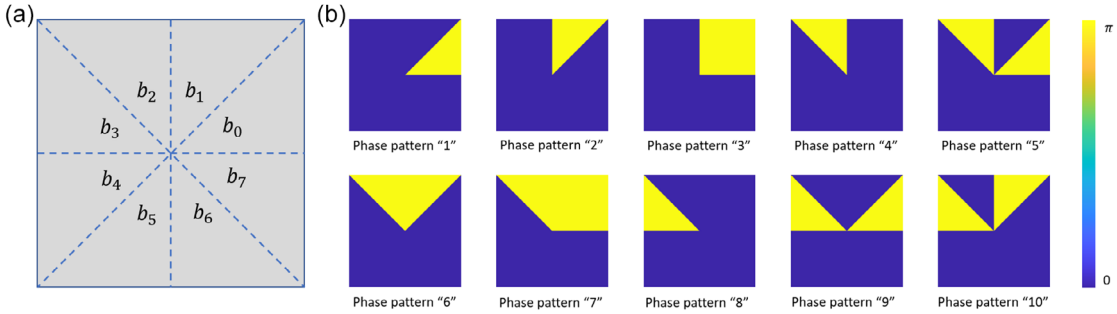

Figure 3. a) System aperture divided into $q = 8$ sectors and b) phase masks corresponding to $k = 1$–10.

approximated to a linear correlation for the NWD. As mentioned earlier, NWD is compared with linear Wiener deconvolution; hence, we mention the following formula for the LWD:

$$I_{\mathrm{L,k}}(\bar{\boldsymbol{r}}) = I_{\mathrm{k}}(\bar{\boldsymbol{r}}) \otimes \hat{p}_{\mathrm{k}}(\bar{\boldsymbol{r}}) = [t(\bar{\boldsymbol{r}}) * p_{\mathrm{k}}(\bar{\boldsymbol{r}})] \otimes \hat{p}_{\mathrm{k}}(\bar{\boldsymbol{r}}) + N_{\mathrm{D}}(\bar{\boldsymbol{r}}) \otimes \hat{p}_{\mathrm{k}}(\bar{\boldsymbol{r}}) = t(\bar{\boldsymbol{r}}) * \tilde{\delta}(\bar{\boldsymbol{r}}) + N'_{\mathrm{P,k}}(\bar{\boldsymbol{r}}) + N'_{\mathrm{D,k}}(\bar{\boldsymbol{r}}) \tag{9}$$

Equation (8) and (9) are similar but not identical. The deconvolution PSFs are different, and because of the optimization process of NWD, the noise terms $N_{\mathrm{P,k}}(\bar{\boldsymbol{r}})$ and $N_{\mathrm{D,k}}(\bar{\boldsymbol{r}})$ of Equation (8) are assumed to be lower than the noise terms of Equation (9) $N'_{\mathrm{P,k}}(\bar{\boldsymbol{r}})$ and $N'_{\mathrm{D,k}}(\bar{\boldsymbol{r}})$.

The operation of averaging in MIND can reduce the noise terms of Equation (8) significantly if the averages of the noise functions $N_{\mathrm{P,k}}(\bar{\boldsymbol{r}})$ and $N_{\mathrm{D,k}}(\bar{\boldsymbol{r}})$ are zero or close to zero. In that case, the final image of the MIND process is

$$I_{\mathrm{N}}(\bar{\boldsymbol{r}}) = \sum_{k}^{K} I_{\mathrm{D,k}}(\bar{\boldsymbol{r}}) = \sum_{k}^{K} [t(\bar{\boldsymbol{r}}) * \tilde{\delta}(\bar{\boldsymbol{r}}) + N_{\mathrm{P,k}}(\bar{\boldsymbol{r}}) + N_{\mathrm{D,k}}(\bar{\boldsymbol{r}})] \cong K \cdot t(\bar{\boldsymbol{r}}) * \tilde{\delta}(\bar{\boldsymbol{r}}) \cong K \cdot t(\bar{\boldsymbol{r}}) \tag{10}$$

and the final image of the MILD process is

$$I_{\mathrm{L}}(\bar{\boldsymbol{r}}) = \sum_{k}^{K} I_{\mathrm{L,k}}(\bar{\boldsymbol{r}}) = \sum_{k}^{K} [t(\bar{\boldsymbol{r}}) * \tilde{\delta}(\bar{\boldsymbol{r}}) + N'_{\mathrm{P,k}}(\bar{\boldsymbol{r}}) + N'_{\mathrm{D,k}}(\bar{\boldsymbol{r}})] \cong K \cdot t(\bar{\boldsymbol{r}}) * \tilde{\delta}(\bar{\boldsymbol{r}}) \cong K \cdot t(\bar{\boldsymbol{r}}) \tag{11}$$

In the next section, we discuss the simulation results of MIND.

3. Simulation Results

The imaging system shown in Figure 1 was simulated in MATLAB software. The ground truth object used in the simulation is an image of size 500×500 pixels padded with a zero matrix to dimensions of 2000×2000 pixels (**Figure 4**a). Zero padding ensures that the object is within a limited region on the object plane. It is also necessary to increase the resolution of the frequency domain.[1] The parameters used in the simulation are an object distance of $z_{\mathrm{o}} = 20$ cm, a focal length of lens L_{A} of $f_{\mathrm{A}} = 20$ cm, a diameter of iris $D = 0.04$ cm, a focal length of lens L_{B} of $f_{\mathrm{B}} = 30$ cm, a separation distance between the L_{A} and L_{B} of $d = 20$ cm, and a camera distance of $z_i = 30$ cm. The simulation is performed for the first eighty-five ($K = 85$) distinct binary phase patterns in the system's aperture for each of the state objects, and the intensity PSF is recorded. As the numerical aperture of the system decreases, the intensity of the signal and SNR decreases. The detection of the camera is governed by Poisson statistics,[44] and with a small aperture in the system, the detected image is considerably blurred, as shown in Figure 4b. To simulate the experimental conditions, a noise distribution governed by Poisson statistics is added in the simulation to the image of the object and to the PSF of the system using the MATLAB imnoise (·) function.[1]

In addition to the reference-free entropy defined in Equation (5), for additional comparisons between techniques, we used the SSIM.[48] Unlike entropy, the SSIM measures the quality of the reconstructed image on the basis of the original object as a reference. The greater the SSIM is, the greater the similarity between the two images. The SSIM is based on the computation of three terms, namely, the luminance term (l), the contrast term (c), and the structural term (s). The overall index is a multiplicative combination of the three terms.

$$\mathrm{SSIM}(A, B) = [l(A, B)]^{\alpha} \cdot [c(A, B)]^{\beta} \cdot [s(A, B)]^{\gamma} \tag{12}$$

where $l(A, B) = \frac{2\mu_A\mu_B + C_1}{\mu_A{}^2 + \mu_B{}^2 + C_1}$, $c(m, n) = \frac{2\sigma_A\sigma_B + C_2}{\sigma_A{}^2 + \sigma_B{}^2 + C_2}$, and $s(m, n) = \frac{\sigma^{AB} + C_3}{\sigma^A\sigma^B + C_3}$

where μ_{A} and μ_{B} are the local means, σ_{A} and σ_{B} are the standard deviations, and σ_{AB} is the cross-covariance for images A and B. If $\alpha = \beta = \gamma = 1$ (the default for exponents) and $C_3 = C_2/2$ (the default selection of C_3), the index simplifies to

$$\mathrm{SSIM}(A, B) = \frac{(2\mu_A\mu_B + C_1)(2\sigma_{AB} + C_2)}{(\mu_A{}^2 + \mu_B{}^2 + C_1)(\sigma_A{}^2 + \sigma_B{}^2 + C_2)} \tag{13}$$

We used the inbuilt function SSIM (A, B) in MATLAB to calculate the SSIM between the original and recovered objects.

The binary phase masks used in the system's aperture in states $k = 1$–5, the respective output images (I_{k}), the intensity PSFs (p_{k}), and the images recovered via linear Wiener deconvolution are shown in **Figure 5**, from top to bottom. The best recovered image in each state is considered the one with the minimum entropy. Wiener deconvolution in regular imaging with an open aperture cannot recover the fine details (Figure 4d) of the original object. Figure 5 demonstrates that high-resolution features lost by limited-aperture imaging are

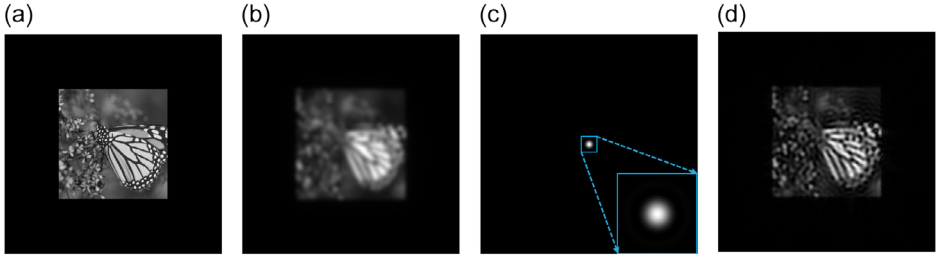

Figure 4. a) Butterfly as a ground truth object used in the simulation, padded with zeros to dimensions of 2000×2000 pixels, b) image of the object obtained by the diffraction-limited imager, c) point spread function of the regular imaging system with added noise, central region of 70×70 pixels (inset), and d) the image recovered with Wiener deconvolution. The entropy is 5.26343.

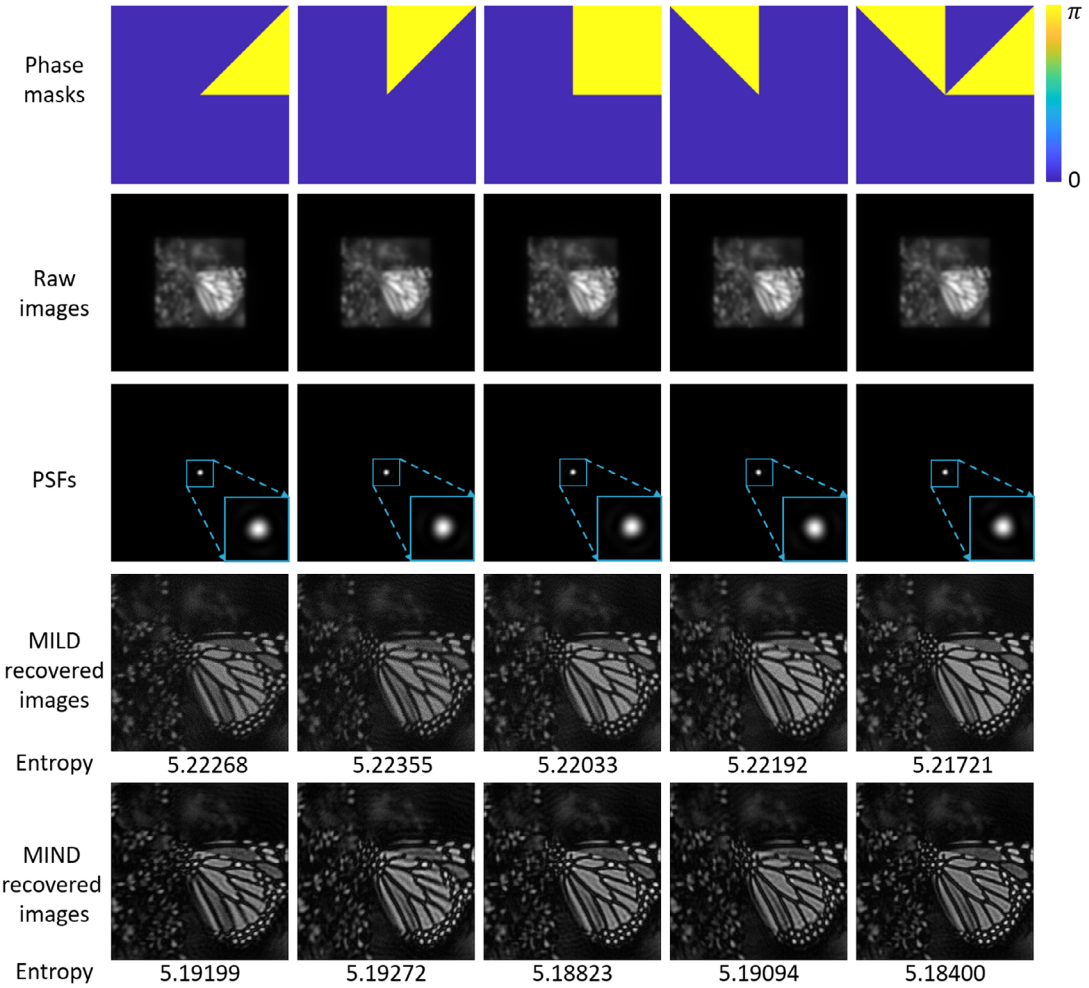

Figure 5. The first five ($k = 1$–5) binary phase masks (first row), raw images (second row), and (third row) PSFs (central regions of 70 × 70 pixels are the insets) in the simulations, along with images recovered using LWD (fourth row) labeled with entropy and NWD (fifth row), are labeled with entropy. The optimal values of o and r for these phase masks are $o = 0.95$ and $r = 1$.

restored in the recovered image, but there are still some artifacts in these recovered images.

In MIND, the raw image for each state of the system's aperture is deblurred using the nonlinear deconvolution expression given in Equation (4). The optimal parameters o, r, and w are searched in the abovementioned ranges. The recovered objects for the system's aperture state $k = 1$–5 are shown in the lowest row of Figure 5. Comparing the two lowest rows of Figure 5, it is clear that nonlinear deconvolution further minimizes the entropy of the recovered object beyond the entropy values of MILD, although noise also persists in the deblurred images in the lowest row of Figure 5.

Next, we reduce the noise level by averaging the resulting images of the three compared methods. The final image reconstructed by averaging multiple linear and nonlinear deconvolutions following imaging with a binary phase pattern is compared with the average of multiple incoherent Wiener deconvolutions of open aperture imaging. The reconstructed images, with an average of twenty, seventy-five, and eighty-five images, are shown in three rows of **Figure 6**. The SSIM of the reconstructed images is calculated in reference to the original object shown in Figure 4a.

The noise appearing in the single deconvolution outcome is minimized in the average of the deconvolved images. The plots of SSIM and entropy versus the number of averaged images are shown in **Figure 7** and **8**, respectively. In the system with an open aperture (Figure 7a), the SSIM increases from 0.4069 to 0.4070 as the number of images increases, whereas in the cases of MILD (Figure 7b) and MIND (Figure 7c), the SSIM increases and reaches a plateau as the number of images increases. The SSIM increases from 0.22 to 0.50 for MILD, whereas in MIND, it increases from 0.28 to 0.38. Although the SSIM with an open aperture is greater than that of MIND, the resolution is poorer, as demonstrated in a qualitative comparison between the left-hand and right-hand columns of Figure 6.

The entropy increases as the number of images increases in all three cases. In terms of entropy, MIND outperforms the other methods, indicating that its resolution performance is superior. This comparison suggests that MIND indeed has lower entropy

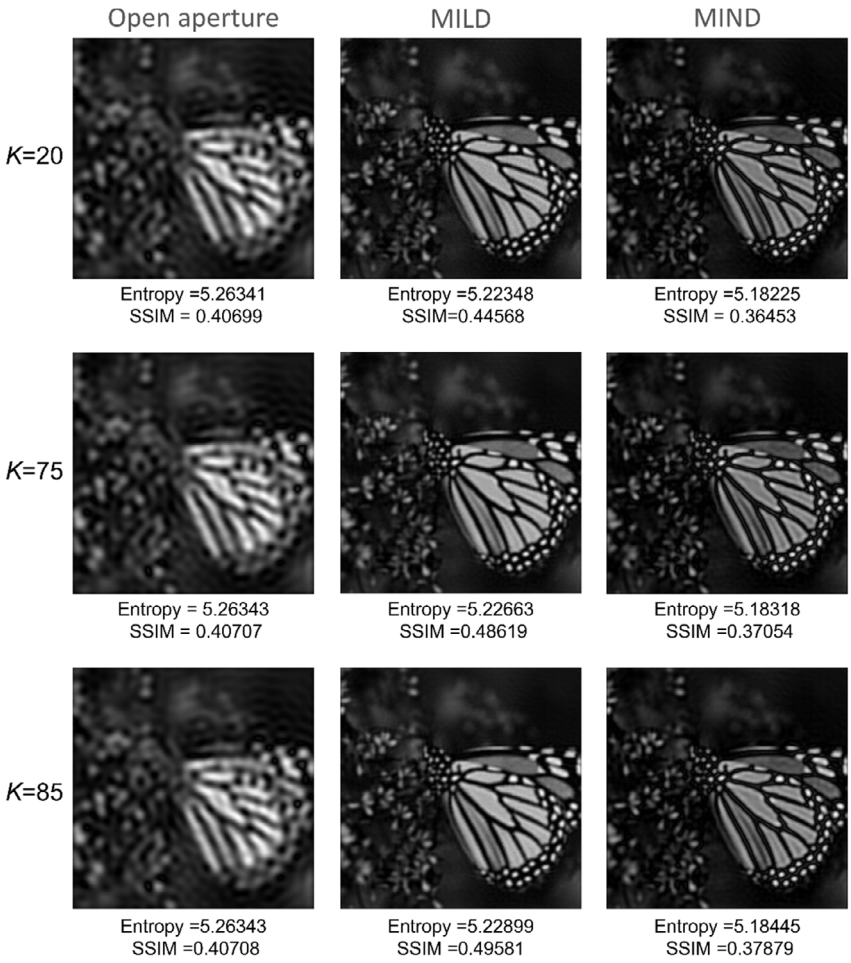

Figure 6. Average over $K = 20$ (first row), $K = 75$ (second row), and $K = 85$ (third row) recovered images of (left-side column) multiple deconvolutions of regular imaging with an open aperture, (middle column) MILD, and (right-side column) MIND in simulations, labeled with entropy and SSIM.

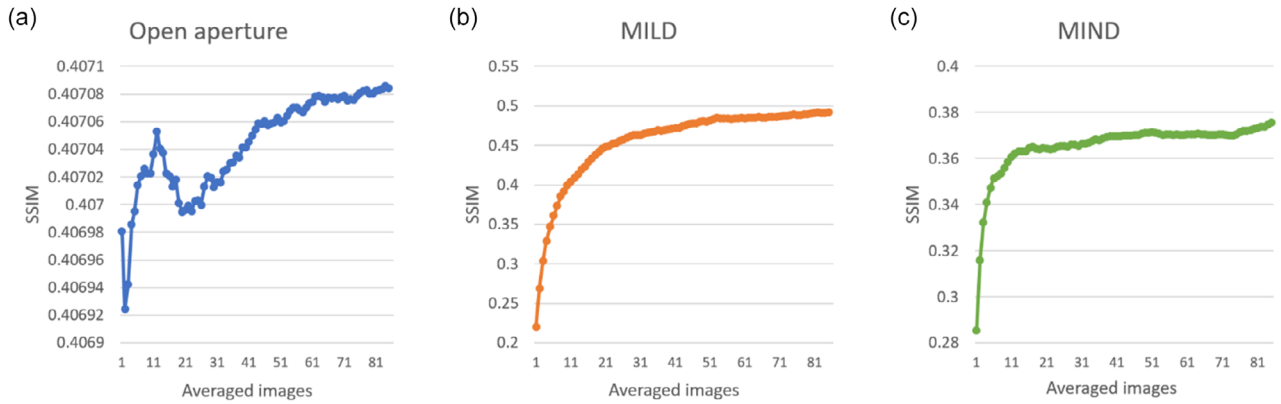

Figure 7. Plots of SSIM versus number of averaged images in simulations for a) multiple LWDs of imaging with open apertures, b) MILD, and c) MIND.

than MILD does and thus improves the resolution beyond the results of MILD; however, after being averaged over multiple recordings, MILD has a greater SSIM than MIND does. Improving the resolution is the primary goal of this research; therefore, the simulation results justify continuing the experiment with a lower number of camera shots because of the plateau beyond $k = 20$. In addition, the resolution should be tested with a more direct measure than entropy, and in the following experiment, the resolution is measured by the visibility of the smallest grating in the image.

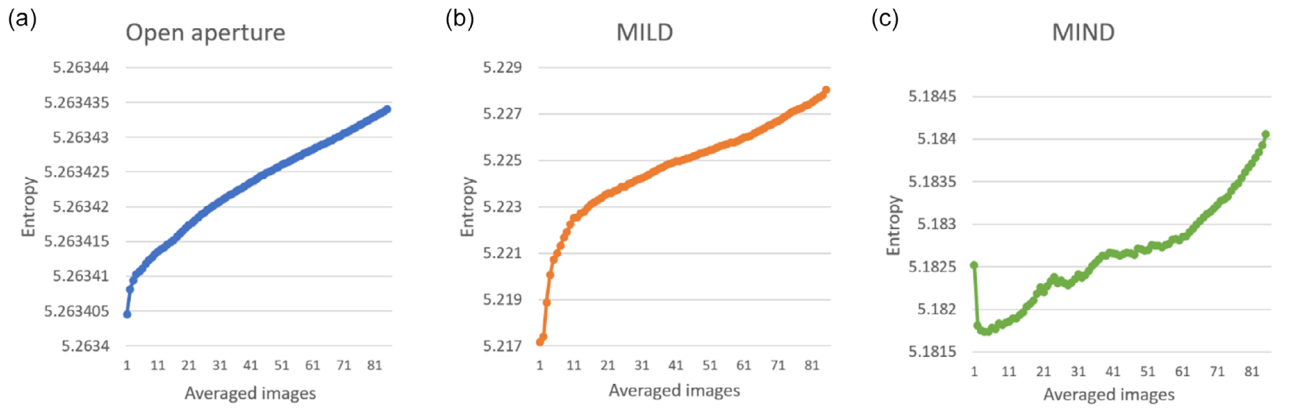

Figure 8. Plots of entropy versus number of averaged images in simulations for a) multiple LWDs of imaging with open apertures, b) MILD, and c) MIND.

4. Experimental Section

A schematic of the experimental setup used in this investigation is shown in **Figure 9**. The setup consists of two identical illumination channels orthogonal to each other with identical light-emitting diodes (LEDs) (Thorlabs LED635L, $\lambda = 635$ nm, $\Delta\lambda = 15$ nm, power = 170 mW) and two identical lenses L_1 and L_2 with a focal length of 5 cm for critical illumination of the targets. In channel 1, elements 2–6 in Group 4 of the United States Air Force (USAF) 1951 positive resolution chart are used as objects. In channel 2, a pinhole (Thorlabs, P5HK) of diameter 5μm is positioned to record the PSF of the system. LEDs are positioned before L_1 and L_2 at $z_1 = 10$ cm, whereas the object and pinhole are kept after L_1 and L_2 at $z_2 = 10$ cm in their respective channels. The object and pinhole are kept at a distance of $z_o = 20$ cm before the collimating lens L_A of focal length $f_A = 20$ cm. The light coming from the pinhole is directed into the lens L_A with a beam splitter (BS_1). An iris with diameter $D = 0.7$ cm is connected to the L_A to limit the aperture of the system. A phase-only reflective-type SLM (Holoeye PLUTO, phase-only modulation, 1920 × 1080 pixels, 8 μm pixel pitch) is placed at a distance $d = 20$ cm after the L_A to display the desired phase mask. For regular imaging, only a diffractive lens with a focal length (f_{DL}) of 30.4 cm is displayed on the SLM, whereas for

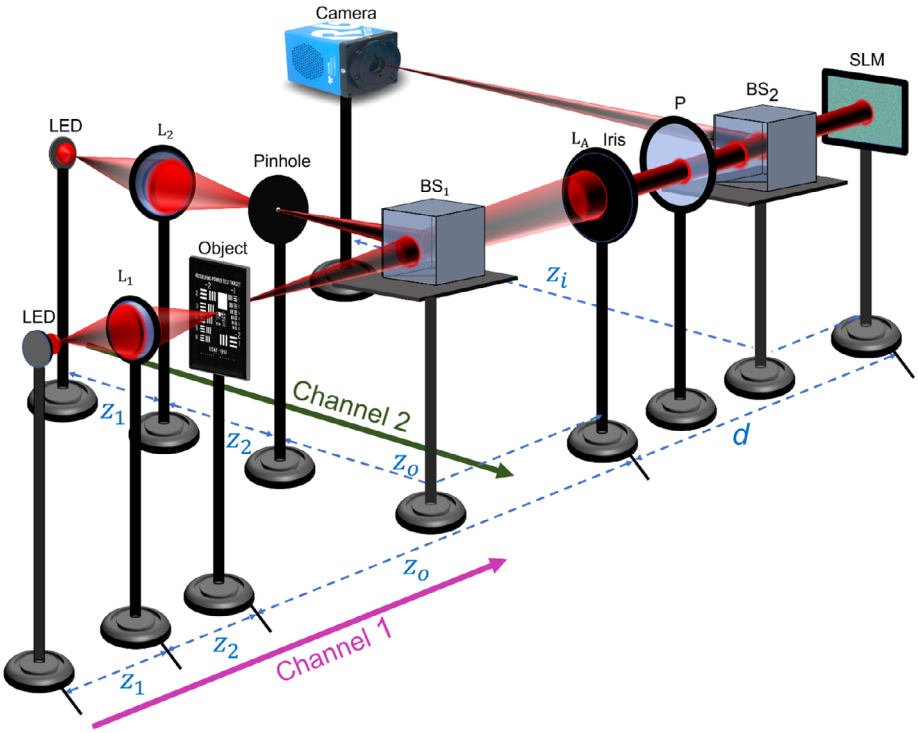

Figure 9. Schematic of the experimental setup used in the study. L_1, L_2, L_A: refractive lenses, BS_1, BS_2: beam splitter, P: polarizer, SLM: spatial light modulator, z_1, z_2, z_o, z_i, d: distances.

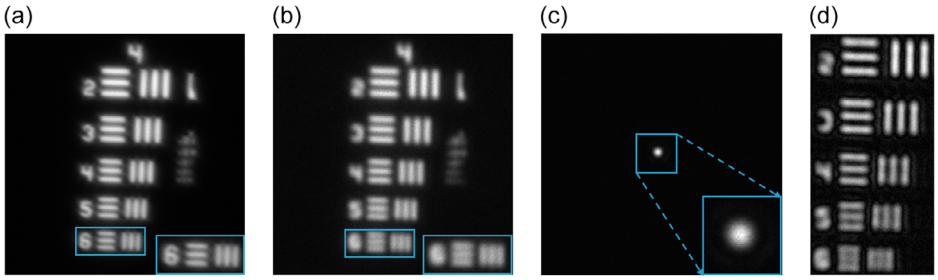

Figure 10. a,b) Raw images in a regular imaging system and element 6 (inset) with (a) an open aperture and (b) an aperture with a diameter of 0.7 cm; c) PSF of the regular imaging system with an aperture with a diameter of 0.7 cm and a central 70 × 70 pixel region (inset) in the experiment; and d) image recovered with linear Wiener deconvolution, with an entropy of 4.3719.

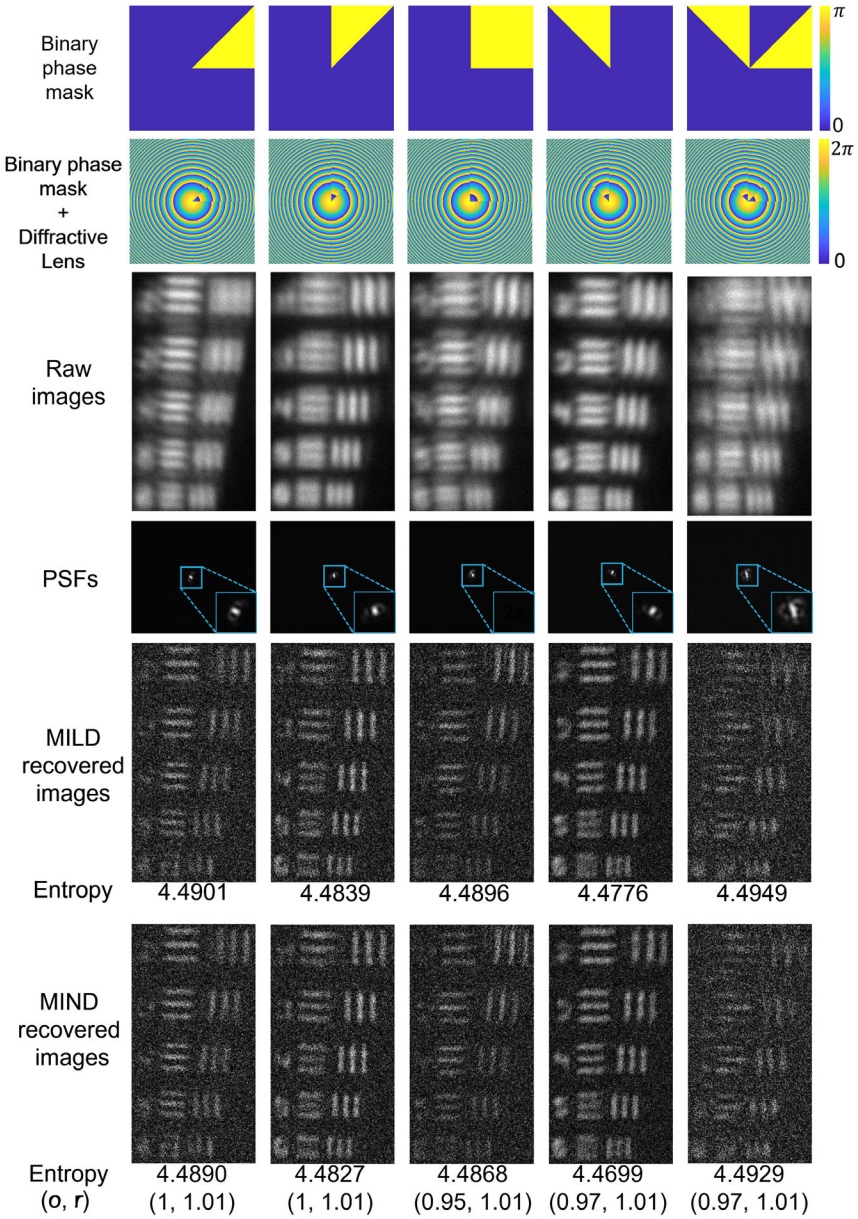

Figure 11. (top row) Central 500 × 500 pixels out of 1080 × 1080 pixels of the SLM of the first five ($k = 1$–5) binary phase masks combined with a diffractive lens, (second row) raw images, (third row) PSFs and 70 × 70 pixel central region (inset) in the experiment, (fourth row) images recovered with LWD labeled with entropy, and (fifth row) images recovered with NWD labeled with entropy and powers (o, r).

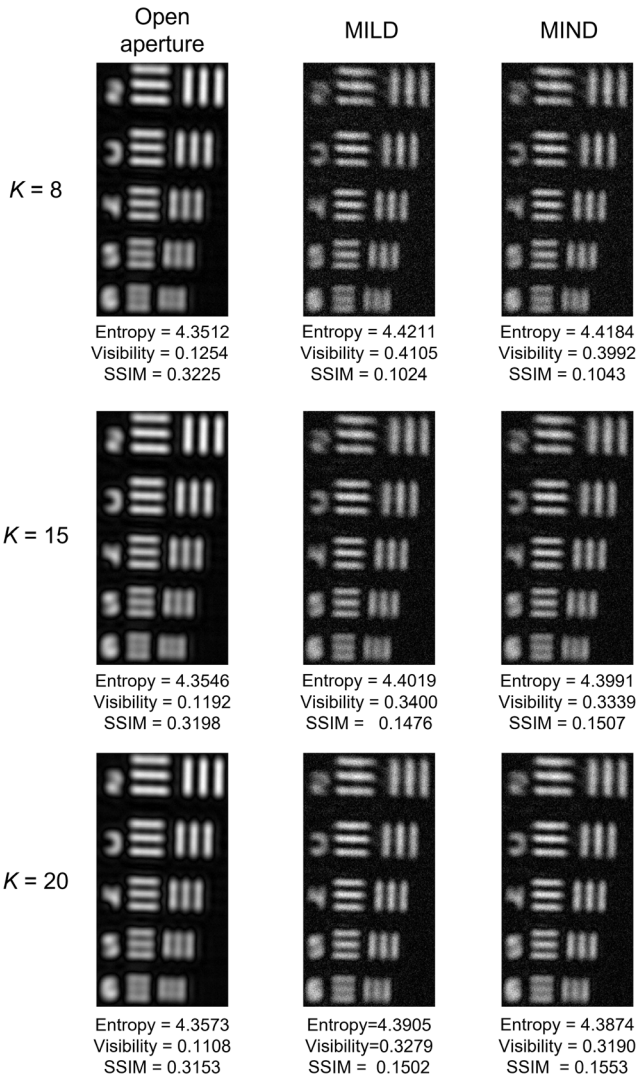

Figure 12. Average of $K = 8$ (first row), $K = 15$ (second row), and $K = 20$ (third row) recovered images using multiple LWDs with open apertures (first column), MILD (second column), and MIND (third column) from raw experimental images, labeled with entropy, visibility and SSIM.

imaging with a binary phase mask, a binary phase pattern of the given state of the system's aperture combined with a diffractive lens with a focal length $f_{DL} = 30.4$ cm is displayed on the SLM. The SLM used in this experiment is a polarization-sensitive device that can modulate only the component of light polarized along the vertical direction. Therefore, a polarizer (P) is maintained at 5 cm after the L_A, which has a polarization axis oriented along the active axis of the SLM. The camera (Retiga-R6, 2688×2200 pixels, 4.54 µm pixel pitch, monochrome) is positioned approximately $z_i = 30.4$ cm from the SLM. The light diffracted from the object is induced on the L_A and collimated during transmission, and collimated light is then incident on the SLM after passing through the polarizer and beam splitter (BS_2). The modulated light reflected from the SLM enters BS_2 and is directed toward the camera and focused on it. **Figure 10**a shows an image of the object in the regular imaging system with an open aperture; all the elements of Group 4 are well resolved. Figure 10b,c shows images of the object and the PSF, respectively, which were recorded in a regular imaging system with an aperture diameter of 0.7 cm. According to Abbe's resolution limit, the minimum resolvable separation between the lines is given by $\lambda/(2\mathrm{NA})$. In the regular imaging system for $\lambda = 635$ nm and $\mathrm{NA} = 0.0175$, the minimum resolvable separation is 18 µm. This implies that the regular imaging system can resolve up to element 5 (separation = 19.69 µm, 25.40 lp mm^{-1}) of Group 4 in the USAF-1951 resolution chart).

To improve the resolution of the image, deblurring is performed with linear Wiener deconvolution when the aperture is open. The object recovered with an entropy of 4.3719 is shown in Figure 10d. For the recovered object, the resolution of element 5 in Group 4 improved, but that of element 6 in Group 4 remained unresolved. In the experiment with LWD, the first twenty binary phase masks ($k = 1$–20) from the library were used in the system's aperture for imaging. **Figure 11** shows, from top to bottom, the phase masks, which are combinations of various binary phases and the diffractive lens, corresponding images of the object, PSFs and recovered images using LWD and NWD. In MIND, NWD is used for deblurring the images for each state of the system's aperture, and the optimal parameters o, r, and w of Equation (4) are searched. The recovered objects for the first five phase masks, labeled with entropy and corresponding (o, r)

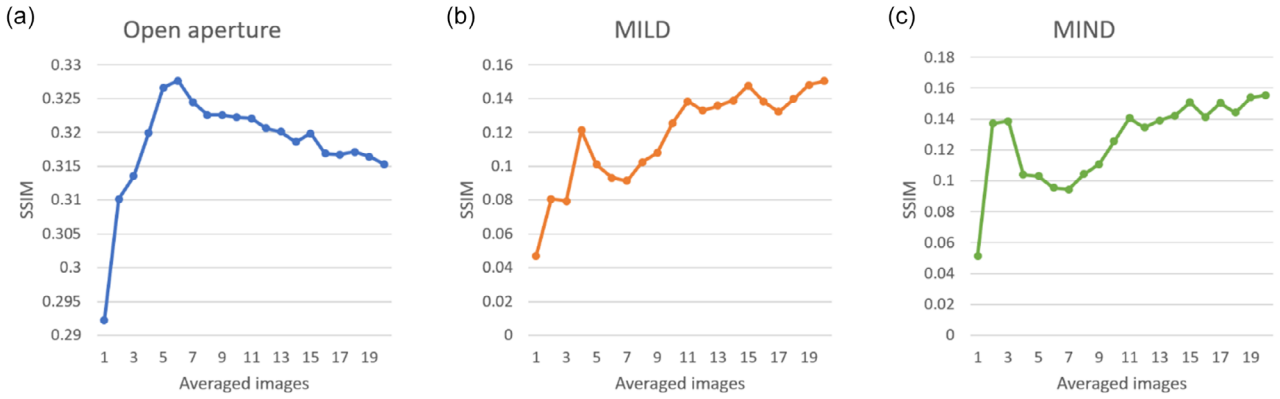

Figure 13. Plots of SSIM versus number of averaged images of a) multiple LWDs of imaging with open aperture, b) MILD, and c) MIND for experimental results.

parameters, are shown in the last row of Figure 11. Nonlinear deconvolution converges to entropies lower than the entropies in linear Wiener deconvolution.

The visibility of the smallest grating, which is calculated as $(I_{max} - I_{min})/(I_{max} + I_{min})$, is considered to indicate the resolution of the system. The SSIM of each average image is calculated in reference to the image obtained without the iris (Figure 10a). The average images reconstructed by averaging multiple deconvolutions, without a phase mask, by MILD and by MIND are compared in **Figure 12**, with averages of 8, 15, and 20 images, from top to bottom, and are labeled with entropy, visibility, and SSIM. Element 6 in Group 4 remains unresolved when averaged over the images obtained without phase masks, and its visibility does not increase above 0.13. The noise in the single deconvolution image is reduced by averaging over images obtained via MILD and MIND. Element 6 in group 4 was resolved in the final reconstruction of the MILD and MIND groups, with averages of 8, 15, and 20 recovered objects, respectively.

The plots for SSIM and visibility versus the number of averaged images are shown in **Figure 13** and **14**, respectively. The SSIM increases as the number of averaged images increases. The SSIM without phase masks increases from 0.2921 to 0.3152, the MILD increases from 0.0469 to 0.1502, and the MIND increases from 0.0513 to 0.1553. Averaging images without any mask is superior in terms of the SSIM. This behavior contradicts the simulation results. This contradiction can be attributed to the use of different reference images. In the simulations, the average SSIM over the recovered objects in each technique is calculated in reference to the original digital object (Figure 4a), whereas in the experiment, the SSIM is calculated in reference to the image recorded in the system with an open aperture (Figure 10a).

As demonstrated in Figure 12 and 14, the visibility of the smallest grating is greater for MILD and MIND than for images without phase masks. In the open aperture, without the phase masks, the entropy increases slightly upon averaging, whereas the entropy decreases in MILD and MIND, as shown in **Figure 15** for the plot of entropy versus the number of averaged images. Although images reconstructed by averaging over images with LWD and NWD have greater entropy than images reconstructed without phase masks do, the resolution of these images, expressed by visibility, is better, indicating that entropy is not a good direct indicator of resolution, as is visibility.

5. Conclusion

MIND is a typical example of a combination of optical and digital processing. Nonlinear deconvolution of every image is performed digitally to increase the resolution, but unfortunately, this

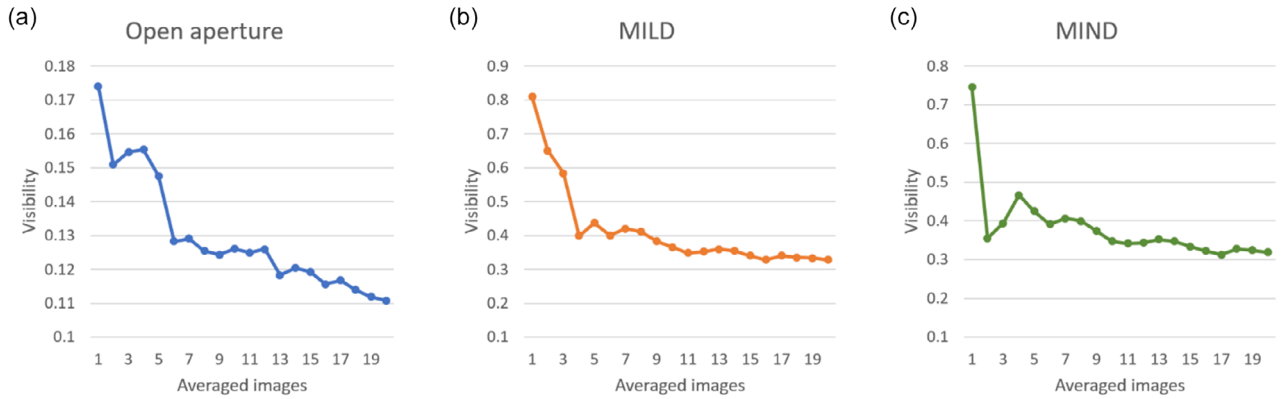

Figure 14. Plots of average visibility versus number of averaged images of a) multiple LWDs of imaging with open aperture, b) MILD, and c) MIND for experimental results.

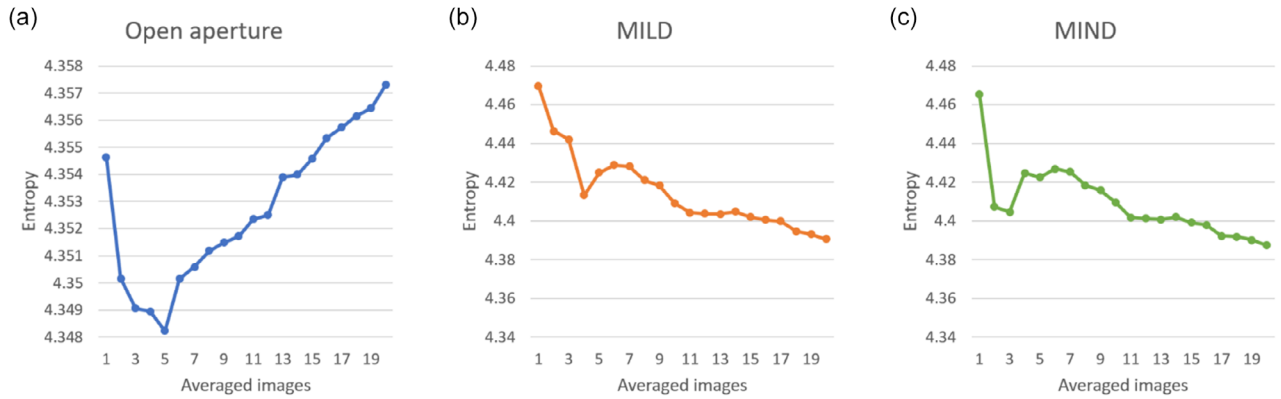

Figure 15. Plots of entropy versus number of averaged images of a) multiple LWDs of open aperture, b) MILD, and c) MIND for experimental results.

technique often produces noisy images. As shown in the present study, this problem is solved herein using the optical part of MIND. In MIND, the SSIM is improved using optical processing by imaging the target with different phase masks displayed on the system aperture and averaging over multiple deconvolved images. The tradeoff between a high SSIM or better resolution can be controlled by determining the number K of recorded images. A small K indicates a higher resolution and lower SSIM than does a large K.

In the present study, MIND was compared with two alternatives. One is multiple linear Wiener deconvolutions always with the same open regular aperture, and the other called MILD is also multiple linear Wiener deconvolutions but with multiple phase masks on the system aperture. MIND always produces better results than does the case without the phase mask in terms of resolution. The comparison between MIND and MILD is less conclusive. The visibility of the smallest element in the resolution chart is slightly greater in MILD, but the SSIM is slightly greater in MIND. Two conclusions can be drawn from the results. First, changes in the system aperture are important and enable the reduction of the noise generated from deconvolution functions. Second, the nonlinearity of the NWD improves the resolution and SSIM but not significantly in comparison to those of the LWD. Therefore, the idea of imaging with multiple apertures significantly improves the resolution, but different types of nonlinear deconvolutions should be further investigated to justify their use. There are many other superresolution methods, but comparisons of these methods are beyond the scope of this study, which is devoted to introducing MIND and demonstrating its results in comparison with the closest techniques. In addition to the concept of MIND, a new deconvolution algorithm, NWD, has been proposed and tested. The NWD was compared with the LWD and NLR and was found to be superior in terms of the SSIM and entropy. The scope of the current study does not enable a comparison of NWD to other deconvolution techniques,[44,51] and among other things, these comparisons will probably be performed in the future.

An important advantage of the proposed method is the ability to add an electro-optical system of MIND or MILD to any existing imaging system. In that case, the digital camera should be disconnected from the existing optical system, and the MIND unit can be inserted between the output of the optical system and the digital camera. This property might make MIND attractive for many existing optical imaging systems. MIND can be attached as a subsystem for improving the resolution beyond the diffraction limit without sacrificing any system resources other than increasing the number of camera shots. Moreover, MIND can be added to many other superresolution methods, especially to those from the second category of increasing the effective numerical aperture. There is no contradiction between MIND and the methods of the second category, which effectively extend the numerical aperture and thus widen the spatial bandwidth. MIND, on the other hand, modifies the effective shape of the MTF but under the restriction that the spatial bandwidth of the system is unchangeable. Hence, MIND can improve the resolution further beyond that achieved by other methods or, alternatively, can improve the SNR achieved by those methods. Finally, MIND emphasizes the advantages of using SLM in optical imaging systems in general[40,52,53] and in optical microscopy.[20]

Acknowledgements

J.P.D. and J.R. were supported by the Israel Innovation Authority under MAGNET under grant no. 79555. V.A. was funded by the European Union's Horizon 2020 Research and Innovation Programme grant agreement no. 857627 (CIPHR).

Conflict of Interest

The authors declare no conflict of interest.

Author Contributions

Jawahar Prabhakar Desai: conceptualization, methodology, validation, writing—original draft, and visualization. **Vijayakumar Anand**: conceptualization and review and editing. **Joseph Rosen**: supervision, conceptualization, and writing—review and editing.

Data Availability Statement

The data that support the findings of this study are available from the corresponding author upon reasonable request.

Keywords

multishot imaging, nonlinear deconvolution, resolution enhancement, Wiener deconvolution

Received: August 15, 2024
Revised: December 25, 2024
Published online: March 2, 2025

[1] R. Gonzalez, R. Woods, S. Eddins, *Digital Image Processing Using MATLAB*, Pearson Education, Inc., Upper Saddle River, New Jersey **2004**.
[2] T. Takahashi, Y. Miyazaki, N. Takeuchi, T. Tanaka, T. Terasawa, *Jpn. J. Appl. Phys.* **2006**, *45*, 5404.
[3] Rayleigh, *London Edinburgh Dublin Philos. Mag. J. Sci.* **1879**, *8*, 261.
[4] E. Abbe, *J. R. Microsc. Soc.* **1882**, *2*, 460.
[5] F. Le Clerc, M. Gross, L. Collot, *Opt. Lett.* **2001**, *26*, 1550.
[6] J. H. Massig, *Opt. Lett.* **2002**, *27*, 2179.
[7] A. Bulbul, J. Rosen, *Photon. Res.* **2021**, *9*, 1172.
[8] J. Desai, R. Kumar, J. Rosen, *Opt. Lett.* **2022**, *47*, 4012.
[9] M. G. L. Gustafsson, *J. Microsc.* **2000**, *198*, 82.
[10] M. G. L. Gustafsson, L. Shao, P. M. Carlton, C. J. R. Wang, I. N. Golubovskaya, W. Z. Cande, D. A. Agard, J. W. Sedat, *Biophysical J.* **2008**, *94*, 4957.
[11] M. Saxena, G. Eluru, S. S. Gorthi, *Adv. Opt. Photon.* **2015**, *7*, 241.
[12] Y. Kashter, A. Vijayakumar, Y. Miyamoto, J. Rosen, *Opt. Lett.* **2016**, *41*, 1558.
[13] V. Mico, Z. Zalevsky, P. García-Martínez, J. García, *Appl. Opt.* **2006**, *45*, 822.
[14] G. Indebetouw, Y. Tada, J. Rosen, G. Brooker, *Appl. Opt.* **2007**, *46*, 993.
[15] M. R. Rai, A. Vijayakumar, J. Rosen, *Opt. Lett.* **2019**, *44*, 1572.
[16] J. P. Desai, J. Rosen, *Opt. Lasers Eng.* **2024**, *174*, 107988.

[17] G. Toraldo di Francia, *Nuovo Cimento Suppl.* **1952**, *9*, 426.
[18] G. Boyer, M. Sechaud, *Appl. Opt.* **1973**, *12*, 893_1.
[19] Z. S. Hegedus, V. Sarafis, *J. Opt. Soc. Am. A* **1986**, *3*, 1892.
[20] J. Rosen, N. Siegel, G. Brooker, *Opt. Express* **2011**, *19*, 26249.
[21] N. Dubey, J. Rosen, *Sci Rep* **2022**, *12*, 4544.
[22] A. Bulbul, N. Hai, J. Rosen, *Opt. Express* **2021**, *29*, 42106.
[23] J.-A. Conchello, *J. Opt. Soc. Am. A* **1998**, *15*, 2609.
[24] F. Sroubek, G. Cristobal, J. Flusser, *IEEE Trans. Image Process.* **2007**, *16*, 2322.
[25] E. A. Mukamel, H. Babcock, X. Zhuang, *Biophysical J.* **2012**, *102*, 2391.
[26] R. W. Gerchberg, *Opt. Acta* **1974**, *21*, 709.
[27] H. Stark, P. Oskoui, *J. Opt. Soc. Am. A* **1989**, *6*, 1715.
[28] J. G. Walker, *Opt. Acta: Int. J. Opt.* **1983**, *30*, 1197.
[29] M. E. Testorf, M. A. Fiddy, *Adv. Imag Electron Phys.* **2010**, *163*, 165.
[30] E. Betzig, G. H. Patterson, R. Sougrat, O. W. Lindwasser, S. Olenych, J. S. Bonifacino, M. W. Davidson, J. Lippincott-Schwartz, H. F. Hess, *Science* **2006**, *313*, 1642.
[31] S. T. Hess, T. P. K. Girirajan, M. D. Mason, *Biophys. J.* **2006**, *91*, 4258.
[32] M. Rust, M. Bates, X. Zhuang, *Nat. Methods* **2006**, *3*, 793.
[33] B. Huang, W. Wang, M. Bates, X. Zhuang, *Science* **2008**, *319*, 810.
[34] O. Tamm, V. Tiwari, S. Gopinath, A. S. J. F. Rajesway, S. A. Singh, J. Rosen, V. Anand, *IEEE Access* **2024**, *12*, 76955.
[35] L. Lu, J. Sun, S. Kan, C. Zuo, in *Proc. SPIE 10462, AOPC 2017: Optical Sensing and Imaging Technology and Applications*, Beijing, China, October **2017**, p. 104624R.
[36] L. Pei, Q. Lv, Y. Liu, J. Wang, in *Proc. SPIE 10423, Sensors, Systems, and Next-Generation Satellites XXI*, Warsaw, Poland, September **2017**, p. 104231T.
[37] B. Wang, C. Zuo, J. Sun, Y. Hu, L. Zhang, in *Proc. SPIE 11396, Computational Imaging V*, California, United States, May **2020**, p. 113960P.
[38] B. Wang, Y. Zou, C. Zuo, J. Sun, Y. Hu, in *Proc. SPIE 11761, Fourth Int. Conf. on Photonics and Optical Engineering*, Xi'an, China **2021**, October 2020, p. 1176111.
[39] K. Liang, B. Wang, C. Zuo, in *Proc. SPIE 12523, Computational Imaging VII*, Orlando, Florida, United States, June **2023**, p. 125230G.
[40] S. Mukherjee, A. Vijayakumar, J. Rosen, *Sci Rep* **2019**, *9*, 17670.
[41] M. R. Rai, A. Vijayakumar, J. Rosen, *Opt. Express* **2018**, *26*, 18143.
[42] C. Liu, T. Man, Y. Wan, *Appl. Opt.* **2020**, *59*, 1769.
[43] V. Anand, T. Katkus, S. Hock Ng, S. Juodkazis, *Chin. Opt. Lett.* **2021**, *19*, 020501.
[44] J. Rosen, V. Anand, *Opt. Express* **2024**, *32*, 1034.
[45] X. Yu, Z. Wang, X. Cheng, L. Zhao, X. Li, Y. Sun, *Opt. Lett.* **2024**, *49*, 482.
[46] A. V. Oppenheim, J. S. Lim, *Proc. IEEE* **1981**, *69*, 529.
[47] A. Dhawan, R. Rangayyan, R. Gordon, *Appl. Opt.* **1985**, *24* 4013.
[48] S. S. Channappayya, A. C. Bovik, C. Caramanis, R. W. Heath, *IEEE Trans. Image Process.* **2008**, *17*, 857.
[49] J. Mait, G. Euliss, R. Athale, *Adv. Opt. Photon.* **2018**, *10*, 409.
[50] J. W. Goodman, *Introduction to Fourier Optics*, Roberts & Co., Englewood, Colorado **2005**.
[51] V. Anand, M. Han, J. Maksimovic, S. H. Ng, T. Katkus, A. Klein, K. Bambery, M. J. Tobin, J. Vongsvivut, S. Juodkazis, *Opto-Electron. Sci.* **2022**, *1*, 210006.
[52] M. Zhang, Y. Wan, T. Man, W. Zhang, H. Zhou, *Opt. Lasers Eng.* **2024**, *173*, 107929.
[53] Y. Wang, H. Wang, C. Zhou, X. Han, S. Liu, X. Lu, J. Di, L. Zhong, *Opt. Lett.* **2023**, *48*, 2732.